Received: 2 November 2021 | Revised: 14 April 2022 | Accepted: 25 April 2022 | Published on: 20 May 2022

DOI: 10.1002/gamm.202200011

ORIGINAL PAPER

Multi-scale characterization of granular media by in situ laboratory X-ray computed tomography

Matthias Ruf[1] | **Kianoosh Taghizadeh**[1,2] | **Holger Steeb**[1,3]

[1]Institute of Applied Mechanics (CE), University of Stuttgart, Stuttgart, Germany

[2]Multiscale Mechanics (MSM), University of Twente, Enschede, The Netherlands

[3]SC SimTech, University of Stuttgart, Stuttgart, Germany

Correspondence
Matthias Ruf, Institute of Applied Mechanics (CE), University of Stuttgart, Pfaffenwaldring 7, D-70569 Stuttgart, Germany.
Email: matthias.ruf@mechbau.uni-stuttgart.de

Funding information
German Research Foundation (DFG), Grant/Award Numbers: STE 969/13-1, STE-969/16-1, 327154368

Abstract

Investigations of biphasic monodisperse soft (rubber) and stiff (glass) particle mixtures under hydrostatic conditions show an interesting behavior with regard to the effective stiffness. P-wave modulus measured by acoustic wave propagation at ultrasonic frequencies showed a significant decline while more soft particles are added, that is, higher rubber volume fractions, due to a change in the microstructure of the granular medium. However, for small volume fractions of soft particles, it could be observed that the P-wave modulus is increasing. This result cannot be explained by classical mixture rules or effective medium theories. For the understanding of those effects, a detailed insight into the microstructure of the granular medium is necessary. To gain this information and link it later back to the measured effective mechanical properties, high-resolution micro X-ray computed tomography (μXRCT) imaging is a well-established tool. With μXRCT imaging, the granular microstructure can be visualized in 3D and characterized subsequently. Combining classical effective characterization methods with μXRCT imaging can help to solve a variety of multi-scale problems. Performing the characterization step in situ, meaning inside the laboratory-based μXRCT scanner, has the advantage that exactly the same samples are mechanically characterized and visualized. To address the mentioned observation above, we designed a low X-ray absorbing oedometer cell with integrated broadband piezoelectric P-wave transducers which enables this kind of investigation inside a laboratory-based μXRCT scanner. The focus of this contribution is on the general experimental methodology which can be transferred to other multi-scale problems. It starts with a description of the image acquisition and ends with the post-processing of the in situ acquired image data. To demonstrate this, cylindrical samples consisting of the same monodisperse rubber and glass particle mixtures that were studied before under hydrostatic stress conditions are considered. Selected results are presented to explain the single steps.

KEYWORDS

granular media, wave propagation, X-ray computed tomography

1 | INTRODUCTION

Granular mixtures are of interest for a large number of fields, materials, and applications, including mineral processing, environmental engineering, geomechanics, and geophysics, and have received a lot of attention in the last decades. A specific example in geotechnical engineering is the increasing incorporation of recycled materials (e.g., shredded or granulated rubber, crushed glass) often used into conventional designs and soil improvement projects [4,12,25]. Moreover, sophisticated mixtures of asphalt and concrete are widely used to construct roads [14,15,48,61,63].

Probing a granular media with (ultra) sound waves gives useful information on the state, the structure and the mechanical properties of the bulk media as there is a one-to-one relation between a wave speed and small-strain stiffness of packings. Estimation of stiffness has traditionally been made in a triaxial apparatus using precise displacement transducers or resonant column devices [1,42]. However, these methods have a disadvantage of destructing samples, whereas ultrasonic measurements (by propagation of an elastic wave) are widely accepted for their rapid, nondestructive, and low-cost evaluation methods. Earlier studies using a wave propagation technique have shown that the dissipative, elastic and lightweight properties of materials (like soils, asphalt, etc.) can be enhanced by deliberately adding dissipative, soft, light inclusions of various types and compositions. Therefore, such a tailored system with improved material properties leads to new application designs.

To study this systematically, the simplest synthetic granular medium is a biphasic mixture of monodisperse soft and stiff particles. In [55], such mixtures under different hydrostatic stresses as well as for different volume fractions were investigated. Measured P-wave moduli showed a significant decline while more soft particles are added, that is, higher rubber volume fractions, due to a change in the microstructure of the granular medium. However, for small volume fractions of soft particles, it could be observed that the P-wave modulus is increasing which is unexpected and not covered by conventional mixture rules. Based on classical mechanical characterization methods such phenomena can be well observed and allow speculations about the physical explanation. However, these remain pure hypotheses. To understand such effects, it is required to have an insight into the microstructure on the particle scale.

There is a diverse array of experimental imaging techniques which can be exploited in order to investigate particulate systems. One of them is attenuation-based micro X-ray Computed Tomography (μXRCT) [6,7,19,41,51]. μXRCT imaging is in general a nondestructive imaging technique that offers the possibility to visualize the internal structure of objects. In contrast to other microscopy imaging methods like optical microscopy, it provides a 3-dimensional (3D) representation of the investigated sample. The method is based on the physical effect of X-ray attenuation which depends among other things on the atomic number and consequently on the chemical composition in each material point. The final, so called reconstructed 3D volume resulting from an μXRCT scan is typically represented as a stack of 2-dimensional (2D) gray value images. Through subsequent post-processing of the 3D raw image data, different material phases can be identified and subsequently segmented [16,40,44,57]. Based on the segmented 3D volume, quantifications on different length scales can be performed. One example to be mentioned on the macroscopic level is the determination of the volume fractions of the individual phases as well as their distribution. But it is also possible to obtain detailed quantities such as the coordination number of individual particles in the case of granular materials. Consequently, experimental results and observed phenomena obtained by classical characterization methods can be better and more comprehensively understood by help of μXRCT.

If μXRCT imaging is combined with classical mechanical characterization methods and performed at the same location we talk about in situ μXRCT imaging [5]. In situ imaging in contrast to running the experiments ex situ in sequential order allows that exactly the same sample is mechanically characterized and visualized. In particular, for granular media, this makes sense since each packing is more or less unique. Motivated by the example mentioned above, within this contribution the general methodology is described how such experiments can be performed in a laboratory μXRCT system. A comparable experiment was recently performed by [62]. However, the focus was on a mixture consisting of monodisperse sapphire spheres with radii between 94 and 103 μm subjected to uniaxial compression, and the experiment was performed in a synchrotron radiation facility instead of a laboratory-based setup used in the present investigation.

In the following, we start with a short overview of image-based characterization using XRCT. The combination (in situ) of this method with the traditional ultrasonic through-transmission measurement technique is the focus of Section 3. We apply this to investigate the identical monodisperse particulate systems as in [56] consisting of weak (rubber) and stiff (glass) particles of different volume fractions. We show a possible realization including the required hardware as well as the overall workflow. Based on this, some selected results of the investigation are provided in Section 4 to give a motivation of what is in general possible. The acquired experimental data for one selected mixture is open access published for

demonstrative purposes. The proposed in situ workflow is discussed in Section 5. A summary of the presented work is given in Section 6.

2 | IMAGE-BASED CHARACTERIZATION USING XRCT

The capability which μXRCT as a nondestructive imaging technique offers are meanwhile well known in many research domains and it is becoming more and more a routine microscopy technique [8,11,23,24,29,31,45,51,52]. The method is based on the revolutionary discovery of X-ray radiation by Wilhelm Röntgen in 1895 [41]. X-rays are high-energy electromagnetic waves with a wavelength in the range of 0.01–10 nm. They have a long absorption length and interact with matter through different mechanisms (photoelectric effect, Compton scattering, Rayleigh/Thomson scattering, and pair production) [7]. Depending on the material penetrated, X-rays are attenuated to different degrees. Assuming a monochromatic X-ray beam, the Beer–Lambert law formulates mathematically the transmitted intensity I of an X-ray beam penetrating an object along the straight ray path from 0 to $\tilde{s}$ by

$$I(\tilde{s}) = I_0 \mathrm{e}^{-\int_0^{\tilde{s}} \mu(s)\mathrm{d}s}, \tag{1}$$

where I_0 is the initial intensity of the X-ray beam and $\mu(s)$ are the unknown local linear attenuation coefficients along the ray path [6,7,51]. If an object is irradiated from one side and the attenuated X-ray beam is measured on the opposite side by an X-ray detector, a so-called radiogram or projection image results. The distribution of the X-ray intensity I is typically represented as a gray value image as displayed in Figure 1A showing one projection image of a cylindrical sample containing monodisperse soft (rubber) and stiff (glass) particles. According to Equation (1), each pixel of such an image represents the intensity I of all attenuated X-ray photons which are captured by the specific sensor pixel during the adjusted exposure time. The darker the gray value the less the intensity I and vice versa in the radiogram. Since each pixel contains just the integral information for one specific X-ray path, it is not possible to back-calculate the unknown linear attenuation values in the material points from one radiogram. However, if a sufficiently large set of projections is taken from different directions, compare Figure 1B, enough information is available to calculate the attenuation coefficient for each material point, compare Figure 1C. The 3D distribution of the calculated attenuation coefficient then represents the inner structure of the investigated object. It is to mention, due to different reasons, that the absolute values of the 3D images are mostly only correlating with the theoretical attenuation coefficients and are not identical.

The general method for the determination of the 3D structure based on numerous projection images is called reconstruction [6,19]. To capture projections from different directions, in μXRCT imaging typically the sample is rotated, compare Figure 1A,B. The number n of required equidistant projection angles φ_i over one turn of the sample correlates with the number of detector pixel columns. The size/discretization of the 3D volume is given by the resolution of the detector. The base area (x- and y-direction) corresponds with the number of detector pixels in the horizontal direction and the maximum height (z-direction) with the number of vertical detector pixels, compare Figure 1C. Corresponding to the term pixel in 2D, in 3D the term voxel is used [40]. Assuming an identical voxel edge length, the edge length of one voxel is given by the ratio of the detector pixel size and the applied geometric magnification $M_{\mathrm{geo.}}$. The adjustment of the magnification in a cone beam system is performed by geometric magnification. If we assume the source-detector-distance (SDD) is fixed, the geometric magnification $M_{\mathrm{geo.}}$ is adjusted by varying the source-object-distance (SOD) and is given by the ratio $M_{\mathrm{geo.}} = \mathrm{SDD}/\mathrm{SOD}$. The maximum theoretically achievable spatial resolution correlates with the underlying focal spot size of the used X-ray source for the adjusted power setting [51]. A micro-focus X-ray source typically has a focal spot size in the micrometer range and results in a theoretical system resolution which is also in the micrometer range.

For the reconstruction itself, it is distinguished between two groups of reconstruction techniques. On the one side, there are analytical reconstruction techniques and on the other side algebraic ones, for example, [6,19]. While the first group of methods tries to solve the inverse problem analytically, the second group treats it as an optimization problem. Both have their respective advantages and disadvantages. The shape of the X-ray beam has a significant influence on the reconstruction, in particular for the analytical techniques. The ideal case of a parallel X-ray beam is only present in beamlines of synchrotron radiation facilities [37] and not given in laboratory μXRCT systems. To account for the conical beam shape in laboratory μXRCT systems, the so-called FDK algorithm is mostly applied. The FDK approach is a practical analytical cone-beam algorithm which goes back to Feldkamp, Davis, and Kress [10]. Independent of the used reconstruction techniques, the final raw data set consists of a stack of slices called tomograms, compare Figure 1C. The

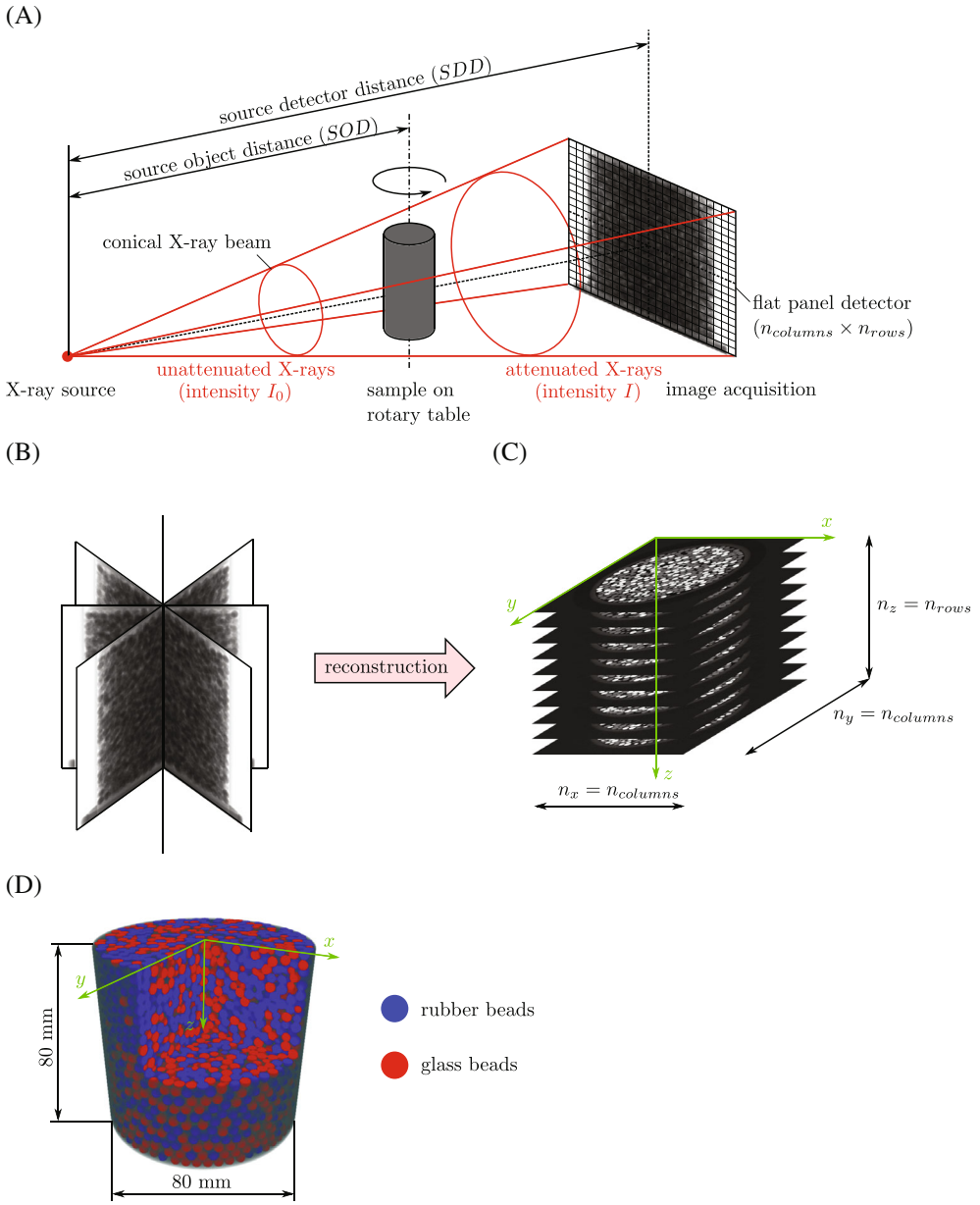

FIGURE 1 Illustration of the principle of attenuation-based X-ray computed tomography (XRCT) imaging based on the scan of a cylindrical sample of monodisperse stiff (glass) and soft (rubber) particles. (A) Cone beam μXRCT, (B) 2D projection images from n equidisant angles φ_i, (C) 3D raw volume, and (D) 3D segmented volume after post-processing

voxel values, typically represented as gray values, represent their influence on X-ray attenuation. The brighter they are the higher their influence on the X-ray attenuation corresponding with the material density. The bright gray voxels in Figure 1C correspond to the stiff (glass) particles and the dark gray ones to the (soft) rubber particles and the nearly black voxels reproduce the air phase. The reconstructed data set contains a certain amount of noise due to the procedure as well as potentially other hardly avoidable artifacts [7,41,51].

By subsequent image processing, based on the 3D raw volume, different kinds of information can be extracted from the data set. For this purpose, a so-called segmentation of the different phases is usually carried out. Segmentation is the partitioning of a gray-scale image into disjoint regions that are homogeneous with respect to some characteristics [16,41,44,57].

In the simplest case, this can be achieved by defining a threshold value, since the individual phases differ in terms of the average gray value. To determine the related threshold values, a histogram of the underlying gray value distribution of the raw data set is usually employed. The most well-known approach based on this scheme is the "Otsu

method" [36]. However, due to the intrinsic present noise in the raw data set, incorrect assignment of different individual voxels occurs. To account for this, various filtering techniques are used [16,44,57]. It is worth mentioning that in recent years, more and more image segmentation techniques using machine learning have been proposed as new approaches due to their well-known benefits [20,22]. Which phases have to be separated depends on the scientific question. Exemplary, in Figure 1D, the separation of the soft (rubber) and stiff (glass) particles, as well as the pore space (transparent), is shown.

By repeating the scanning process as well as the image processing, the evolution of physical processes (e.g., deformation, crack initiation, and growth) over time can be observed. The final result is one stack of tomograms (3D image) for each time step. What kind of processes can be observed depends on the required acquisition time for one complete scan. While acquisition times of less than one second for one complete scan are achievable in beamlines of synchrotron radiation facilities [5,13,28,37], the acquisition time in a standard lab-based μXRCT system is between some minutes up to several hours, correlating with the required scan quality. This is one limitation of physical processes which can be studied. However, processes which can be stopped in an equilibrium state are also open for investigation in a laboratory system. For time-resolved scans, the term 4-dimensional (4D) scanning (space + time) is frequently used.

3 | IN SITU EXPERIMENTAL TESTING

The combination of μXRCT imaging with classical mechanical characterization methods is an excellent technique to better understand the behavior of materials as well as physical processes in general, compare [5,49]. In this context often the term "in situ X-ray computed tomography" is used. "In situ" is a Latin phrase and translates literally to "on-site" or "on place" and is the antonym of "ex situ." In the experimental mechanics' context, it describes the way the measurement is taken, highlighting that the measurements are acquired in the same place the phenomenon is occurring without removing/installing the sample each time. Thus, in situ μXRCT means that the mechanical characterization is performed inside the scanner. It offers the possibility to enrich the information on the macroscopic level, for example, resulting from acoustic measurements as demonstrated within this contribution, with information on the microscopic level resulting from 3D imaging. In the following, we provide an overview of the applied workflow and used hardware to investigate particulate systems with acoustic wave measurements combined with in situ μXRCT imaging.

3.1 | Stiffness determination based on wave propagation measurement

Mechanical (sound) waves are disturbances that propagate through space and time in a medium in which deformation leads to elastic restoring forces. This produces a transfer of momentum and energy from one material point to another, usually involving little or no associated mass transport if the amplitude is small enough. The P-wave, or primary wave, is the fastest and the first wave detected by seismographs. They are able to move through both, solid rock as well as through liquids. P-waves are compressional or longitudinal waves that oscillate the ground back and forth along the direction of wave travel, in much the same way that sound waves (which are also compressional) move air back and forth as the waves travel from the sound source to a sound receiver. In a longitudinal wave, the particle displacement is parallel to the direction of wave propagation [30,32,33,47,53].

Quantitative ultrasonic measurement has been widely-used by different disciplines ((geo-)physics, soil and geomechanics, materials sciences, mechanical and civil engineering) to describe the small strain stiffness behavior of a particulate system, as can be found in literature [17,18,50,58]. Velocity testing by through transmission ultrasound methods has gained popularity due to its relative ease of obtaining the modulus of a sample. Figure 2 shows a schematic view of the used low-frequency ultrasound setup integrated into an oedometer cell including its electrical pieces, compare Figures 3 and 4. For our highly attenuating particulate system, it consists of a pair of 100 kHz P-wave broadband piezoelectric transducers (Olympus-Panametrics Videoscan V1011), an ultrasonic square wave pulser/receiver unit (Olympus-Panametrics 5077PR), and a digital oscilloscope (PicoScope 5444B). Piezoelectric transducers are used to determine the small-strain compression stiffness, M, of the granular system by determining the velocity of mechanical waves ("speed of sound") through the tested samples. The transducers are generally used in pairs when one transducer operates as a transmitter and the other as a receiver. The transmitting transducer is generally embedded at one end of the particulate sample and the receiving is, aligned with the transmitter, embedded at the other end. This allows to probe the stiffness of the soil or particulate sample along a given stress path. The transmitting transducer transforms the input

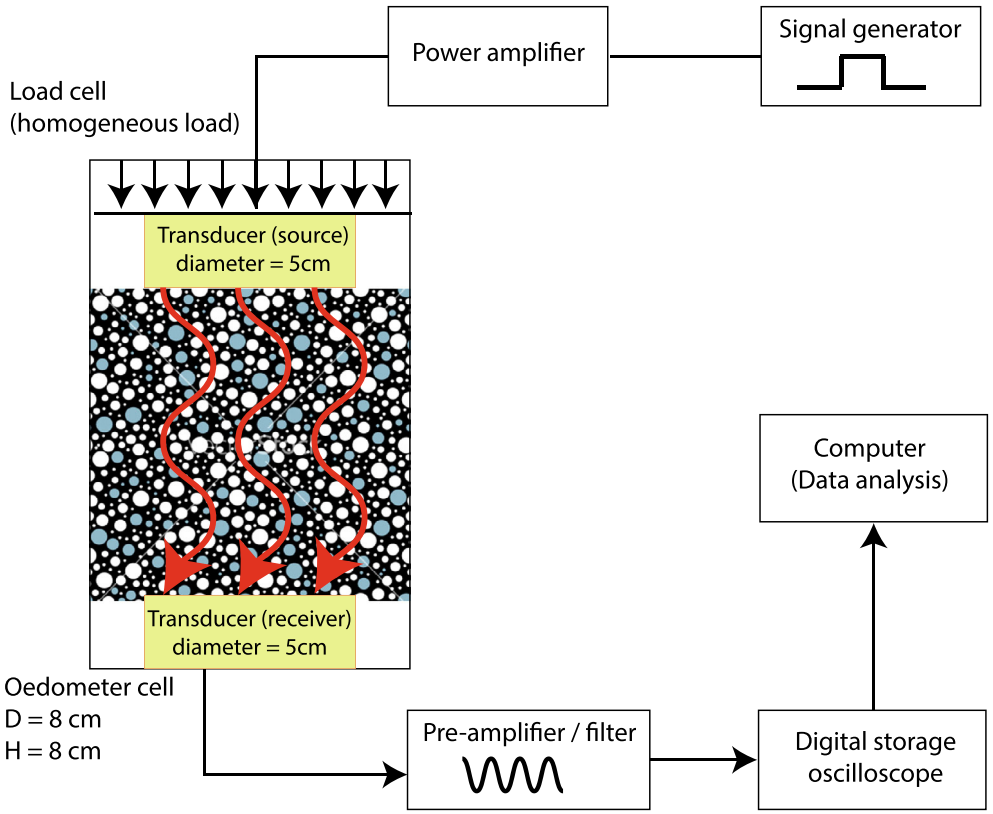

FIGURE 2 Schematic view of wave propagation measurement setup [55]

electric signal to an acoustic wave and sends it through the medium. The receiving transducer receives the propagated mechanical sound wave and transforms it back to an electronical signal which can be acquired by the digitizer, compare [27,43] for technical details on the transducers. Transducers are often incorporated in geomechanical and geophysical laboratory testing equipment such as in triaxial or oedometers cells.

The P-wave velocity (V_P) can be calculated from the travel time (t_P), given the height (H) of the sample in the actual configuration, $V_P = H/t_P$. Knowing the elastic wave velocity (V_P) and knowing the total bulk density (ρ_B) of the particulate system, the longitudinal P-wave stiffness of the sample (M) is determined, $M = \rho_B V_P^2$. In our investigations, the sample consists of monodisperse rubber and glass particles leading to a bulk density $\rho_B = \nu\rho_r + (1-\nu)\rho_g$, where ρ_r and ρ_g are the bulk densities for 100% of rubber and glass particles, respectively. The volume fraction of the rubber particles is denoted with ν.

3.2 | µXRCT system and oedometer cell

The experimental study was performed in an open, modular, and flexible lab-based µXRCT system with an intrinsic large space allowing for the installation of a mechanical testing device required for in situ investigations. A detailed description of the system can be found in [38]. The system presented in [38] was extended by the integration of a load frame for mechanical in situ µXRCT investigations, compare Figure 3A. For this, a Zwick 1445 10 kN Universal Testing Machine (UTM), refurbished from Doli Elektronik GmbH, Germany, and equipped with a modern EDC 222V controlling system, is employed. In the UTM, two rotatory tables with high loading capacities (XHuber 1-Circle Goniometer 411-X3W2) are integrated. The rotatory tables are prestressed with the controlled force $F_{\text{stat.}}$ applied to the sample during the image acquisition process. The X-ray source of the system is an open micro-focus tube with tungsten transmission target (FineTec FORE 180.01C TT) from FineTec FineFocus Technology GmbH, Germany. For the image acquisition, a Dexela detector 1512NDT with GOS-based DRZ Standard scintillator option from PerkinElmer, Inc., Waltham, MA, USA is applied. To perform ultrasonic through transmission measurements in situ, a low X-ray absorbing oedometer cell was designed and manufactured in-house. Compared to a triaxial cell, only the vertical stress in the axial direction is controlled. In Figure 3,

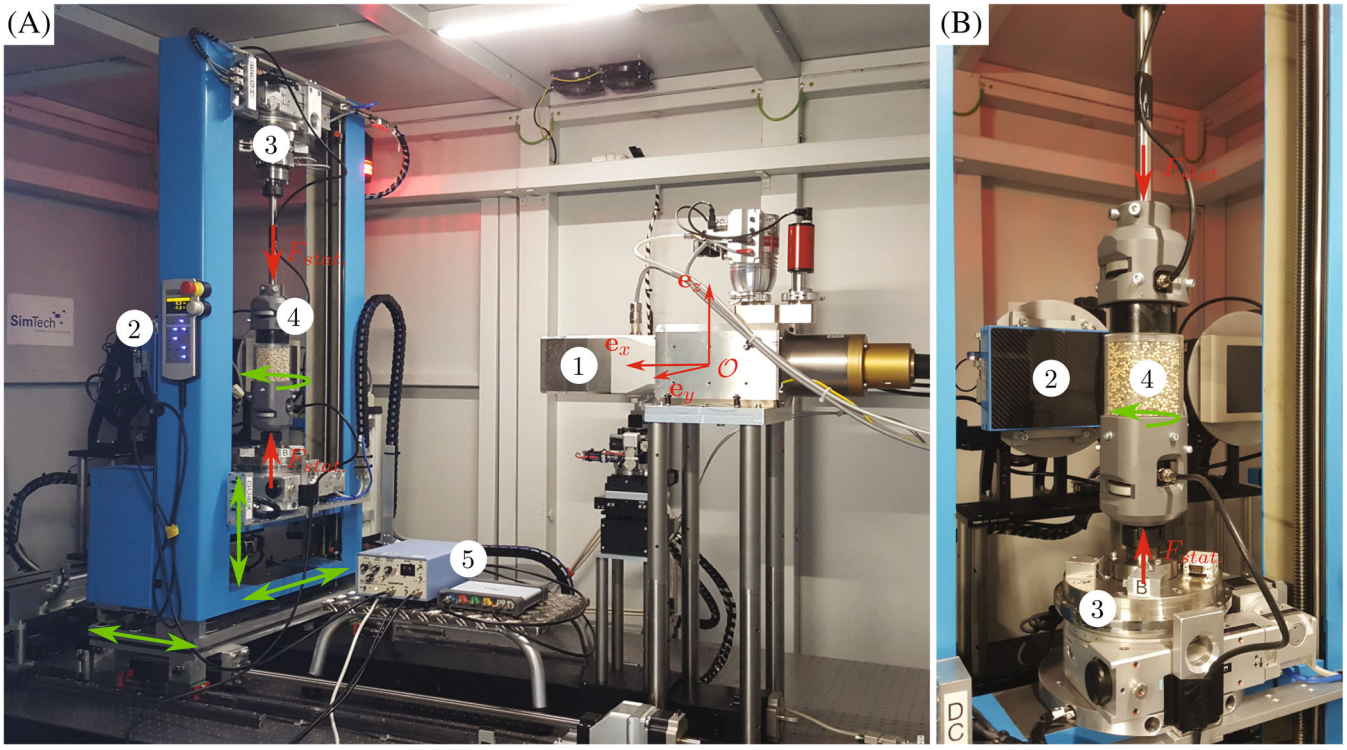

FIGURE 3 Experimental in situ setup: (1) X-ray source, (2) X-ray flat panel detector, (3) universal testing machine with synchronized rotary tables, (4) oedometer cell with integrated P-wave transducers containing monodisperse glass and rubber particles, and (5) square wave/pulser receiver unit and PC oscilloscope for ultrasonic measurements

the oedometer cell installed in the μXRCT-system and loaded by the employed universal testing device is presented. Further, the electrical devices for the ultrasonic testing corresponding to the schematic Figure 2 can be seen. A detailed view of the oedometer cell design is provided in Figure 4. The oedometer cell consists of three components. The top (1) and bottom (3) parts, both with integrated P-wave transducers, transfer the applied axial compression force $F_{\text{stat.}}$ to the sample and results in the axial stresses denoted as pressure $p_{\text{stat.}}$. As transducers, a pair of 100 kHz P-wave broadband piezoelectric transducers (Olympus-Panametrics Videoscan V1011) is employed, compare Section 3.1. For the coupling of the transducers to the poly(methyl methacrylate) (PMMA) holders of the oedometer cell, an adequate couplant fluid is used. On both sides, the wave travels through a 10 mm long PMMA distance, before and after the wave enters and leaves the sample. The contact pressure $p_{\text{cont.}}$ in between the transducers and the PMMA holders can be adjusted by an adjusting wheel. The sample is held in a rigid confining ring (2) made out of PMMA which prevents lateral displacement of the investigated mixture. Between the PMMA ring and the top and bottom part is a small gap in the radial direction to ensure that the emitted waves propagate through the sample. PMMA is used for the confining ring, as it has a very low attenuation coefficient. The inner diameter D of the PMMA ring is 80 mm. The sample height H can be varied from 70 to 80 mm.

To capture the whole cell content (diameter 80 mm; height 80 mm), a geometric magnification $M_{\text{geo.}} = 1.36$ was set for all particulate systems. This leads to a field of view of 106.92 mm × 84.48 mm. Since we are not interested in small features (bead diameter 4 mm) all projection images were acquired in 2 × 2 detector binning mode. This means, that the detector's full resolution of 1944 × 1536 pixels with 74.8 μm pixel pitch and 14-bit pixel depth is reduced to 972 × 768 pixels with a pixel size of 149.6 μm. On one side, this significantly improves the signal-to-noise ratio (SNR), and on the other side, the final tomogram data set size is reduced by factor 8. Both simplify the subsequent image processing significantly without the loss of information required for the presented study. For all scans, an acceleration voltage of 110 kV with an acceleration flux of 110 μA for the X-ray source were set. For all scans, 1440 equidistant projection angles were used in combination with a detector exposure time of 1000 ms. Further, a detector bad pixel compensation as described in [38] was employed using two different projection positions for each projection angle. The final tomogram stacks have a size of 972 × 972 × 768 voxels with the uniform voxel edge length of 110 μm. The 3D reconstruction of all scans was performed with the software Octopus Reconstruction (Version 8.9.4-64 bit) [60] using the filtered back projection (FBP) method [19]

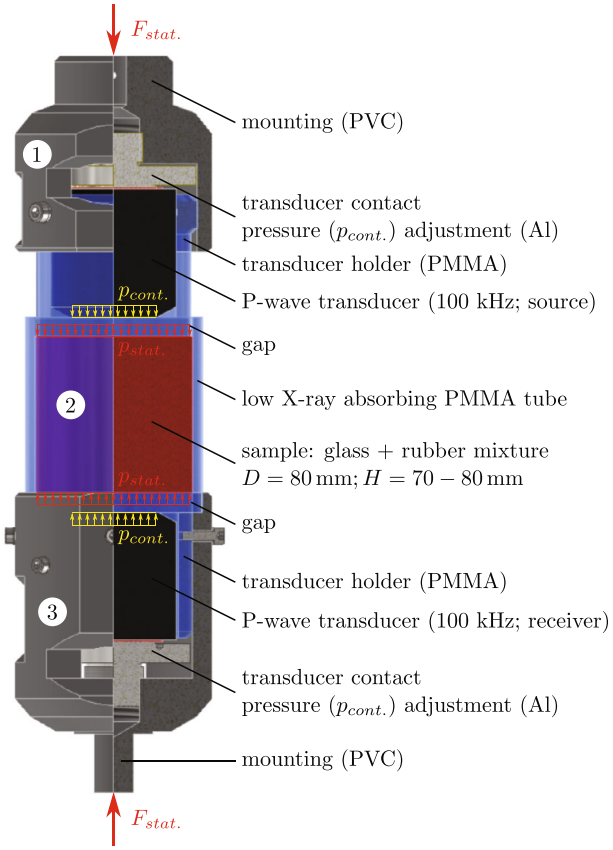

FIGURE 4 Three-quarter section view of the low X-ray absorbing oedometer cell with integrated ultrasonic transducers for in situ measurements

in combination with the FDK reconstruction algorithm [10]. To account for common artifacts in μXRCT imaging (ring artifacts and beam hardening), different types of filters were used. Based on the tomograms, segmentation is performed to distinguish between the rubber and glass beads and the remaining pore space. The segmentation workflow is described in detail in Section 3.3.

3.3 | Image analysis

Here, we present steps taken using the Dragonfly software version 2020.2 for Windows from Object Research Systems (ORS, Montreal, QC, Canada) [34], for the segmentation and the subsequent quantification of mixture samples. An important step before interpreting the data is to identify individual particles. To increase the quality of images and reduce unwanted noise, one can apply different image filtering techniques before segmenting the phases, that is, separating different objects in an image. Here, a 3D-median smoothing function with a kernel size of seven was applied on image stacks. Next, voxels of images were manually divided into three different regions of interest (air, rubber, and glass) which are used as boundaries of objects. After segmenting samples into three separate regions (air, rubber, and glass), watershed transform technique is employed on defined markers of individual particles to label every particle in the separated regimes of rubber and glass. The watershed is a classical region-based algorithm that has its origins in mathematical morphology [3,9,46,59] used for segmentation. Starting from user-defined markers, the watershed algorithm treats pixels values as a local topography (elevation). The algorithm floods basins from the markers until basins attributed to different markers meet on watershed lines. In many cases, markers are chosen as local minima of the image, from which basins are flooded.

Figure 5 shows a z-direction view of a layer of particles prepared at two rubber fractions, $\nu = 0.1$ (left) and 0.5 (right), under 800 N load in the oedometer cell. Light and dark gray pixels represent glass and rubber particles respectively in

the first row. Second row shows the segmented pixels in the regions of interests (rubber (blue) and glass (red)) for which deep learning was employed. Thanks to the watershed transform technique, particles of segmented regions are labeled individually (third row).

3.4 | Investigated particulate samples and measurement workflow

All investigated samples are made of monodisperse glass and rubber beads with 4 mm diameter. Further information on the material characteristics for both, glass and rubber beads, can be found in [55]. Particles are poured carefully into the oedometer cell described in Section 3.2. Samples are prepared at different rubber volume fractions, $\nu = v_r/v_c$, from $\nu = 0$ to 1 in 0.1 increments, where v_r is the volume possessed by the rubber particles and v_c is the total volume of particles in the oedometer cell. All mixtures are tested in the custom-made oedometer cell with the sample height (unloaded) and diameter equal to 80 mm, compare Figures 3 and 4 ex situ without imaging. The prepared samples are uniaxially compressed in the axial direction via the top piston of the oedometer cell in subsequent force increments from $F = 200$ to 1000 N. At each instant step, the system was relaxed for some time at the defined force to overcome the creep behavior of soft particles. Then, at each intermediate load step, a high voltage burst signal (P-wave) is excited from the top cap (the sound source)

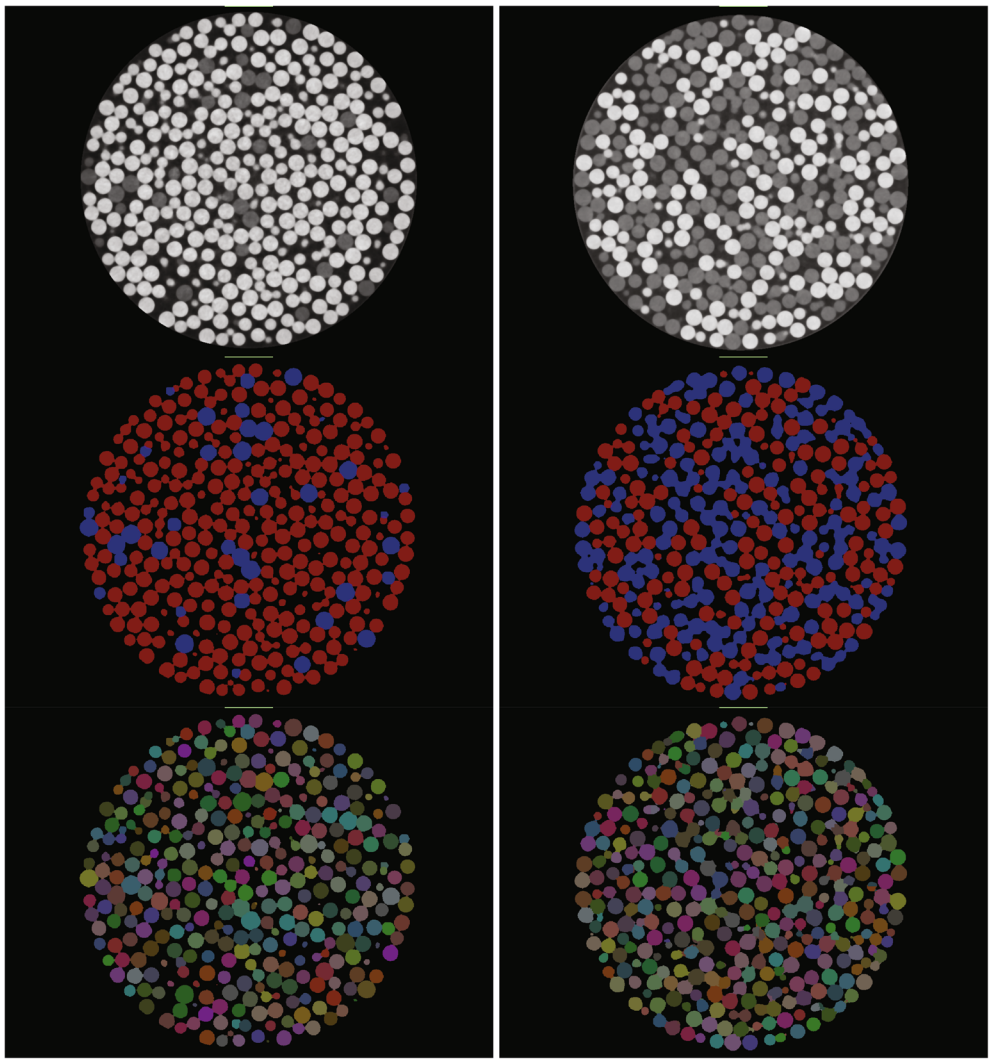

FIGURE 5 A top view of a *xy*-layer of particles for samples prepared with $\nu = 0.1$ (left column) and 0.5 (right column). Top to bottom shows the steps taken from a reconstructed raw image (first row) to segmented (second row), and labeled (third row). The 3D raw dataset for $\nu = 0.5$, here presented with a single slice ("slice_xy_0322.tif"), can be found in [39]

I. In situ data acquisition

1. Static preloading of granular mixture with $F_{stat.}$
2. Determination of mixture stiffness by acoustic wave propagation measurement
   - Traveling time t_P with mixture height $H \Rightarrow$ wave velocity $V_P = H/t_P$
   - Wave velocity V_P with mixture density $\rho_B \Rightarrow$ P-wave modulus $M = \rho_B {V_P}^2$
3. micro X-Ray Computed Tomography (μXRCT) scan of the preloaded mixture (acquisition of projections + 3D volume reconstruction with Filtered Back Projection (FBP))

II. Image data processing

4. Segmentation of soft and stiff particle phase via thresholding (different X-ray attenuation coefficients)
5. Separating of single particles by watershed algorithm $\Rightarrow$ labeling of each particle
6. Extracting information about particle contacts, networks etc.

FIGURE 6 In situ workflow summary

transducer and the bottom transducer collects the signal. To remove the influence of network configurations and user errors on outputs, each experiment was repeated at least 3 times by mounting and dismounting particles into the cell. For the calculation of the system stiffness besides the wave propagation time t_P, the exact height H of the compressed packing is required. This is determined based on the loading protocol of the UTM. Since about 2 h are needed for one μXRCT scan, only a subset of the possible combinations of the parameter space (rubber volume fraction ν and preload $F_{\text{stat.}}$) were scanned in situ. μXRCT imaging was performed for a preload $F_{\text{stat.}} = 400$ N and $F_{\text{stat.}} = 800$ N in combination with rubber volume fractions $\nu = \{0.1, 0.2, 0.3, 0.4, 0.5, 0.6\}$. Otherwise, the procedure is identical to the previously performed ex situ measurements. During the image acquisition, it is switched from force-control to displacement-control to avoid slight movements of the particles due to relaxation processes. The selection is based on previous knowledge from comparable experiments in a triaxial cell without μXRCT imaging [55] as well as the before performed ex situ measurements in the oedometer cell. A summary of the applied in situ workflow is given in Figure 6.

4 | RESULTS—INSIGHT INTO GRANULAR MEDIA

Measurement of ultrasound velocity V_P provides complementary information about material properties, and combined use of velocity and topological structure in seismic analysis provides greater insight into the granular packings. Here, we first report the results on the bulk stiffness of granular mixtures with diverse rubber content obtained by the experimental tests. Particular attention is devoted to the dependence of sound velocity on the applied load and soft-stiff composition of samples, since this is an important controllable experimental parameter [21,26,55]. After that, X-ray images taken during wave propagation are analysed to obtain micro-insights of packings.

4.1 | Material characterization by ultrasonic measurements

Figure 7 shows the compressional modulus M determined for samples prepared with rubber fractions from $\nu = 0.1$ to 0.6 at five different load steps acquired in situ. The underlying data of the mixture with $\nu = 0.5$ (ultrasonic measurement data as well as measured force and displacement data of the UTM) together with the recorded μXRCT dataset (reconstructed data set, projection data set, and metadata) is for illustrative purposes available in [39]. M modulus shows high stiffness for rubber content up to $\nu = 0.3$ where the bulk behavior of samples is highly controlled by the stiff phase. Previous experimental studies under triaxial stress conditions showed already that a small amount of soft particles enhances the effective stiffness of the medium [55]. Thus, the effective stiffness of biphasic monodisperse granular mixtures consisting of stiff and soft particles does not follow a simple mixture rule. The highest modulus is observed at $\nu \approx 0.2$. Thus, granular

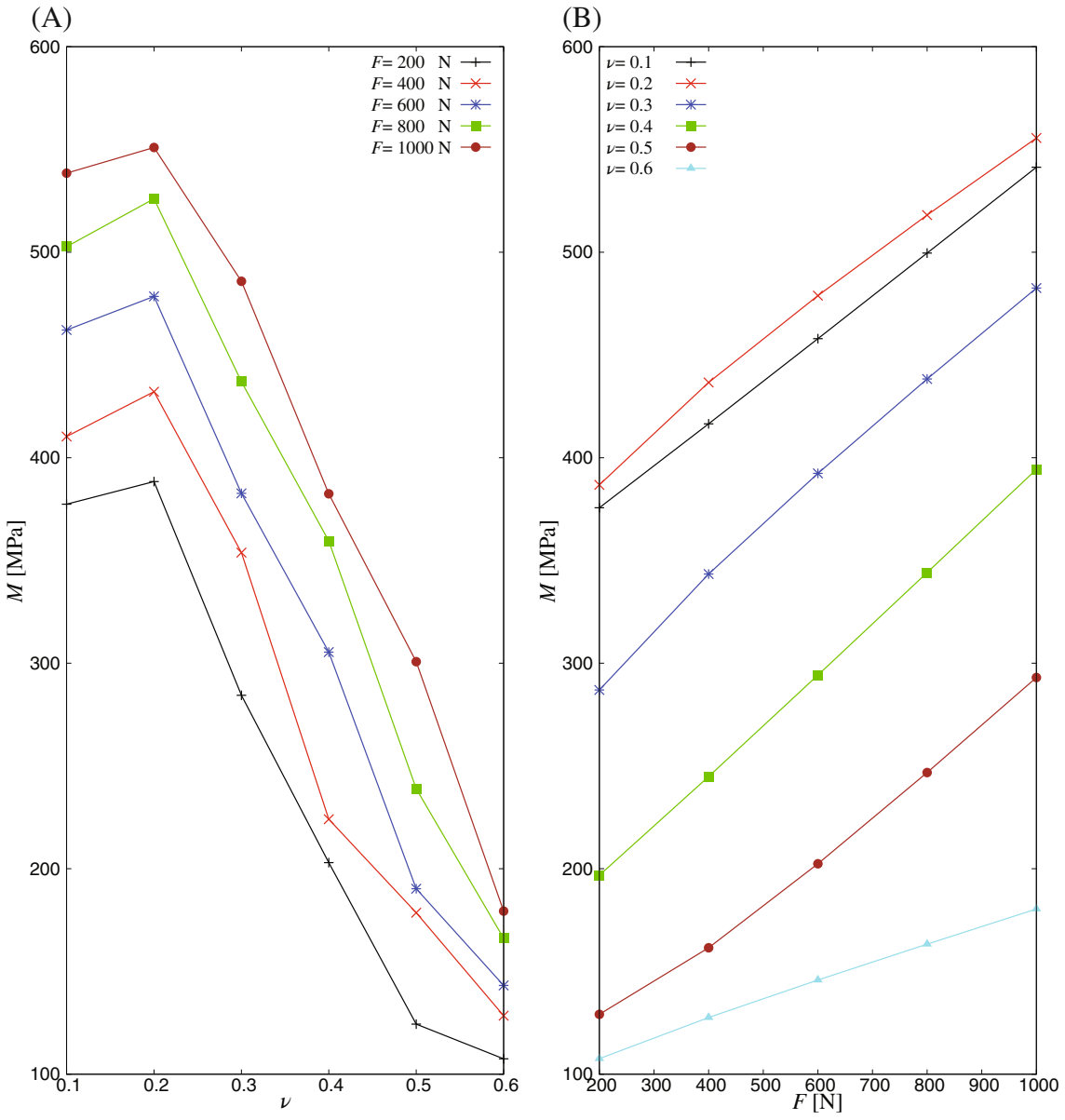

FIGURE 7 (A) In situ measured P-wave modulus M against rubber fraction ν. (B) P-wave modulus against uniaxial applied load from $F = 200$ to 1000 N. The underlying measurement data for $\nu = 0.5$ is provided in [39]. For the full range of mixtures (measurements performed without imaging in a triaxial cell), see [56]

mixtures can be manipulated to obtain aggregates with even higher stiffness, but lighter and more dissipative thanks to rubber, when appropriate external conditions are matched (in this case the pressure) [21]. Increasing the amount of rubber particles, here $0.3 < \nu < 0.6$, reduces the effective stiffness where a phase transition from stiff to soft phase occurs.

4.2 | Image characterization

Progress in the application of μXRCT imaging in the field of geomechanics allows all the individual particles of packings in a test sample to be seen and identified uniquely in 3D. Combining such imaging capabilities with experiments carried out "in situ" within an imaging setup (shown in Figure 3) has led to the possibility of directly observing the topology of packings.

Granular matter has a heterogeneous nature, this is expressed as force chains through the medium. These force chains spread the forces through the contact with another particle [53,54]. This causes that neighboring particles could have forces of different magnitudes and nonisotropic distributions of stress throughout the medium [2]. This heterogeneity is manifest of the fact that granular matter exhibits a strong configuration and history dependence. One of the interesting outcomes of μXRCT imaging of particulate systems is its potential to depict contact networks which provide micro-structural information.

A 3D view of labeled particles is shown in Figure 8A for a sample prepared with $\nu = 0.5$; and the contact network of the sample is illustrated in Figure 8B. Center of particles, marked with different colors, are connected with black lines. The color code of the number of contacts follows as black (zero), magenta (one), blue (two), red (three), green (four), yellow (five), orange (six), and white (above six). Next, to enhance micro-structural investigation, glass and rubber particles are separated as a result of labelling every particles for samples with volume fraction of $\nu = 0.1$ (Figure 9) and 0.5 (Figure 10). Looking at glass (Figure 9A) and rubber (Figure 9B) networks of $\nu = 0.1$, it is not surprising to see the scatter

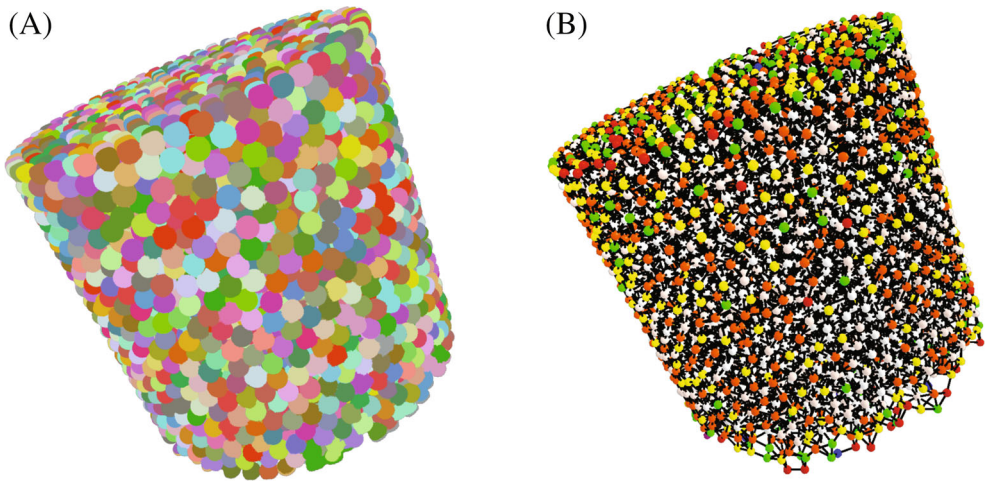

FIGURE 8 (A) 3D view of labeled particles for a sample prepared with $\nu = 0.5$. (B) The network of contacts of the sample in which different particles colors represent a number of contact each particle carries. Particles carrying zero, one, two, three, four, five, six, and above six number of contacts are colored by black, magenta, blue, red, green, yellow, orange, and white, respectively.

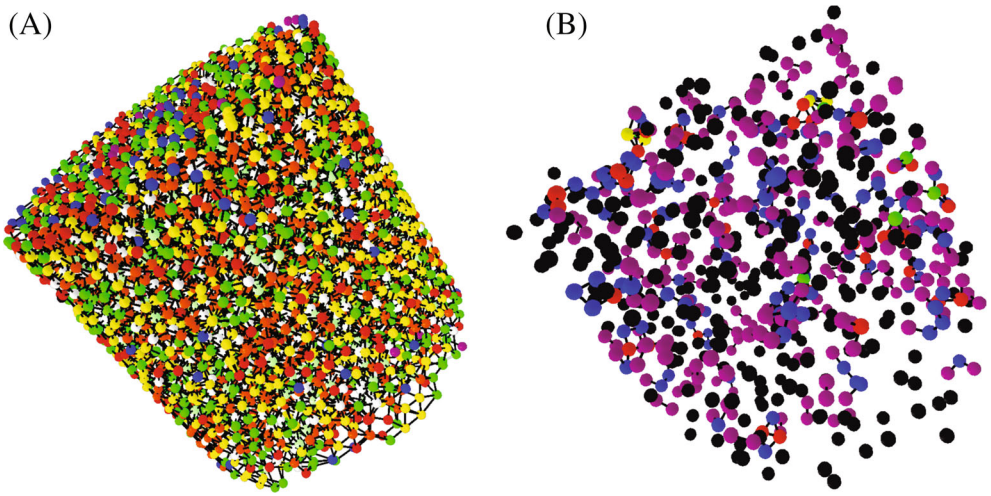

FIGURE 9 3D view of (A) glass and (B) rubber particles network for a sample prepared with rubber fraction $\nu = 0.1$, respectively. Particles center are marked with different colors based on their number of contacts and connected with black lines. Particles carrying zero, one, two, three, four, five, six, and above six number of contacts to the same particle phase are colored by black, magenta, blue, red, green, yellow, orange, and white, respectively.

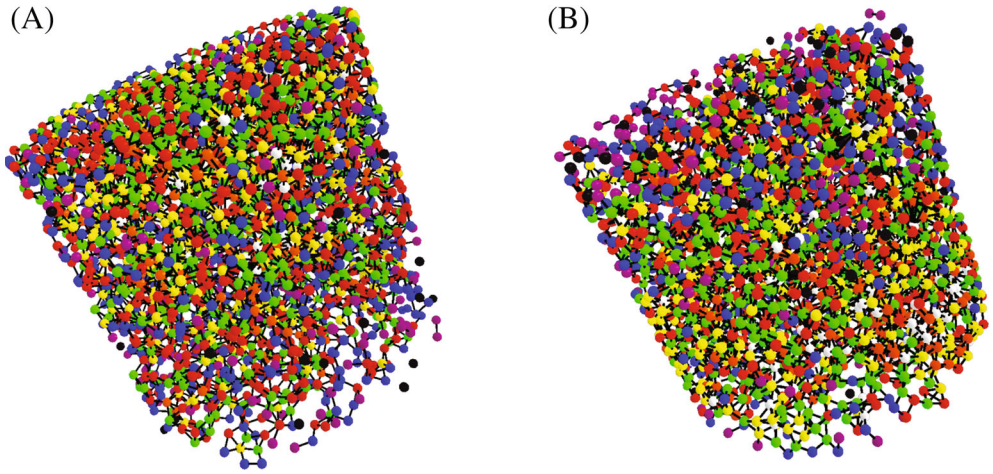

FIGURE 10 3D view of (A) glass and (B) rubber particles network for a sample prepared with rubber fraction $\nu = 0.5$, respectively. Particles center are marked with different colors based on their number of contacts and connected with black lines. Particles carrying zero, one, two, three, four, five, six, and above six number of contacts to the same particle phase are colored by black, magenta, blue, red, green, yellow, orange, and white, respectively.

of rubbers among glass beads. These rubbers which do not carry number of contacts above three are called rattlers. Rattlers do not transfer force between each other as their number of contact are not sufficient to form a chain of particles; whereas, moving to a sample with higher rubber fraction $\nu = 0.5$ (Figure 10), we do not see rattles neither in the glass and nor in the rubber networks. This observation explains why M modulus remains fairly constant for samples with low rubber volume fraction ($\nu \leq 0.3$) in Figure 7 since their bulk behavior is controlled by stiff particles. But in case of intermediate regime, ν between 0.4 and 0.6, forces are distributed among glass and rubber chains which leads to a smaller M modulus.

5 | DISCUSSION

As is almost always the case, no experimental investigation is perfect. The problems that arise must be critically questioned with regard to their influence on the scientific question. The motivation for the presented study was given by investigations of the same kinds of mixtures in a conventional triaxial cell with well-defined boundary conditions [55]. Since it is quite more complicated to design and build such a cell that can be used in an μXRCT device, we went for an oedometer cell. As the results in Figure 7 show, we can observe the same phenomenon. As a consequence, it is an admissible simplification for the problem under investigation.

One common significant uncertainty and difficulty is associated with determining the exact wave propagation time by ultrasonic measurements required to calculate the sample stiffness. Suggested criteria and recommendations vary depending on the installation, application, and input signal. The most common methodology is to interpret the received signal in the time domain. It is typical to consider the first peak at the receiver transducer as arrival time and the required time difference minus the needed time in the other parts as the travel time of the signal within the packings [35] which was consistently done within this study. However, in particular, for high rubber packings, choosing a peak is not easy since the wave contains high-frequency tones raised from the cluster of rubber particles. Thus, a low-pass filter was applied to remove unwanted noises. For high rubber volume fractions, this is nevertheless a difficult undertaking and not completely objective. Although the same experimental protocol and measurement were applied, a user error is inevitable. To account for this, ex situ measurements were repeated three times in the past and are consistent with the in situ acquired data shown in Figure 7.

During the image acquisition period which takes up to 2 h, the piston control of the uniaxial machine was switched from force-control to displacement-control. This was done to avoid slight movements of the particles due to creeping processes caused by the (viscoelastic) rubber particles. As a result, a corresponding relaxation can be observed in the measured force. For instance, for a mixture ratio of $\nu = 0.5$, the measured force (stress) decreased from 400 to 340 N (80 to 68 kPa) and from 800 to 696 N (159 to 138 kPa) which means a reduction of about 15% and 13%. However, this is only slightly

critical with respect to particle movements at least in the range of resolution used. This can be confirmed by the final quality of the 3D images as well as by comparing the in situ ultrasonic measurement results with the before performed ex situ measurements. Consequently, the relatively long μXRCT scan time has no significant influence on the imaging. In the shown concept, the static preload $F_{\text{stat.}}$ is applied using a load frame, here a modified traditional universal testing machine. Consequently, two rotary tables must be used to rotate the prestressed sample. While this concept generally offers extremely great flexibility (uniaxial tension/compression and torsion) compared to specially designed load cells with integrated actuators, compare [5,49] and the literature cited therein, it also presents some difficulties. The major problem is the accurate alignment of the two rotatory tables in the micrometer range. Each eccentricity error leads either to an undefined stress state and/or to bad image quality due to potential movement errors in soft samples since the error is multiplied with the set geometric magnification ($M_{\text{geo.}}$). However, because an extremely low geometric magnification is applied here ($M_{\text{geo.}} = 1.36$) and, in addition, the individual particles are comparatively large with a diameter of 4 mm, this influence is to be classified as minor on the underlying scientific question. Although it is slightly present in the samples with a very low rubber fraction. To get completely rid of this error source the alignment of the rotary tables should be further improved which is technically challenging or alternatively, a load cell with integrated actuator could be employed. However, the latter leads to a significantly more complicated and expensive cell design. Therefore, this approach was intentionally not chosen. Common artifacts in μXRCT imaging (e.g., noise, ring artifacts, system alignment errors, and beam hardening) could be reduced to a minimum by the combined usage of hardware precautions and software-based corrections. In general, it is advantageous to use relatively large particles as in our approach, as this significantly reduces many potential sources of error.

Segmentation of μXRCT data is certainly the most critical step before quantitative analyses. Due to the good quality of the raw datasets (justifying the scanning time of 2 h), and the fact that only three high-contrast phases (air, glass, and rubber) had to be segmented, this could be accomplished with a straight forward traditional workflow. Since the exact composition of each mixture is known (total particle volume and number of particles), the segmentation and subsequent separation of the single particles could be validated quite easily on a global level. The exact deformation of the individual particles is not of interest for the presented study. Consequently, the image processing and the quantification can be judged as very reliable.

In the result part, just some selected 3D visualization of two datasets were shown. Further analysis of the 3D data has to be performed to get more information out of it and to finally link back to the observable effects on the macroscale. Since the general methodology of the experiments was the focus of this work, this was deliberately not presented here.

It can be concluded that the presented in situ setup in combination with the applied workflow is adequate to get a more comprehensive understanding of particulate systems as presented in this contribution. Further, it demonstrates that an investigation of such kinds of questions are accessible with a laboratory-based μXRCT system if some boundary conditions are fulfilled, for example, an intrinsic large space within the system.

6 | SUMMARY

Understanding the response of granular-based systems in applications requires a detailed grasp of the connection between the basic ingredients (particles) and the macroscale properties of the systems considered. These are complex systems and an understanding of the overall behavior cannot be gained by studying individual particles. While significant progress has been made during the last decades on understanding relevant physical mechanisms, there are still many open questions, starting from the physics of particle interactions to general features of multiscale models that will bridge the different spatial and temporal scales of interest. The purpose of this contribution was to describe an in situ characterization approach for the combination of traditional experimental techniques with 3D imaging in order to explore a micro-macro relation of granular assemblies.

The given work started initially with a short overview about attenuation-based μXRCT imaging in Section 2. Based on this, a detailed explanation of how μXRCT and wave propagation measuring technique are combined was demonstrated in Section 3. For this, a low X-ray absorbing oedometer cell with integrated P-wave transducers was designed and built. The cell was integrated into a modular μXRCT-system which was extended by a load frame using a refurbished universal testing machine. This approach enables applying in a flexible manner different kinds of load cases needed for advanced mechanical in situ investigations. A typical approach to segment different material phases of the 3D tomograms was explained step-by-step. The sample material chosen for the study is a composition of monodisperse granular particles,

glass, and rubber beads; not only because of the ubiquity of granular materials but also because it is a paradigm for complex disordered media and the unique characteristics exhibited by various physical phenomena associated with mechanical waves in it (dispersion, scattering attenuation, intrinsic attenuation, diffusion, weak localization, energy transfer across different frequencies, etc.).

In Section 4, the effect of rubber volume content variation of the studied glass-rubber mixtures on the compressive elastic modulus (P-wave modulus) by means of wave propagation at different uniaxial preload levels was shown. It was demonstrated that the modulus of the mixtures can be increased by adding low portions of soft particles since it is dominated by stiff particles. Adding more soft particles into assemblies led to a transition from stiff to soft dominated regime where bulk behavior of samples is mainly controlled by soft phase. The macro behavior of such granular samples can hardly be described without micro information. To gain more insights, μXRCT imaging was performed in situ for two of the five examined preloads. Analyzing images helped to understand the transition mechanism from stiff to soft controlled regime by separating glass and rubber networks. It was found that due to the isolation of rubber particles, rattlers, the samples were dominated by glass grains. Whereas, a sample with 50 % of rubber and glass has distributed number of contacts, fairly, among themselves.

The combination of experimental material characterization and image characterization techniques is a complex procedure that was explained carefully in this article. However, it could be demonstrated what incredible potential it has. In particular, since many problems from the field of mechanics are accessible in laboratory-based μXRCT systems.

ACKNOWLEDGEMENTS

The authors acknowledge the scientific discussion with Stefan Luding. Also, we thank Ralf Plonus for his technical support in modification of devices. M.R. and H.S. acknowledge funding from the German Research Foundation (DFG) through Project No. STE 969/13-1. K.T. and H.S. acknowledge funding by the German Research Foundation (DFG) through the project STE-969/16-1 within the SPP 1897 “Calm, Smooth and Smart.” H.S. thanks the DFG for supporting this work under SFB 1313 (Project No. 327154368). Open Access funding enabled and organized by Projekt DEAL.

CONFLICT OF INTEREST

The authors declare no potential conflict of interests.

ORCID

Matthias Ruf https://orcid.org/0000-0003-0299-5921
Kianoosh Taghizadeh https://orcid.org/0000-0003-3394-3251
Holger Steeb https://orcid.org/0000-0001-7602-4920

REFERENCES

[1] J. H. Atkinson and G. Sallfors, *Experimental determination of soil properties. General report to session 1*, Proc. 10th ECSMFE, Florence, Vol. 3, 1991, pp. 915–956.
[2] D. S. Bassett, E. T. Owens, K. E. Daniels, and M. A. Porter, Influence of network topology on sound propagation in granular materials, Phys. Rev. E **86** (2012), 041306.
[3] S. Beucher, The watershed transformation applied to image segmentation, Scanning Microsc. **1992** (1992), 28.
[4] P. J. Bosscher, T. B. Edil, and S. Kuraoka, Design of highway embankments using tire chips, J. Geotech. Geoenviron. Eng. **123** (1997), 295–304.
[5] J. Y. Buffiere, E. Maire, J. Adrien, J. P. Masse, and E. Boller, In situ experiments with X ray tomography: An attractive tool for experimental mechanics, Exp. Mech. **50** (2010), 289–305.
[6] T. M. Buzug, *Computed tomography*, Springer, Berlin Heidelberg, 2008.
[7] S. Carmignato, W. Dewulf, and R. Leach, Eds., *Industrial X-ray computed tomography*, Springer International Publishing, Berlin, Germany, 2018.
[8] V. Cnudde and M. Boone, High-resolution X-ray computed tomography in geosciences: A review of the current technology and applications, Earth Sci. Rev. **123** (2013), 1–17.
[9] H. Digabel and C. Lantuéjoul, *Iterative algorithms*, Proc. 2nd Eur. Symp. Quant. Anal. Microstruct. Mater. Sci. Biol. Med., Vol. **19**, 1978, pp. 8.
[10] L. A. Feldkamp, L. C. Davis, and J. W. Kress, Practical cone-beam algorithm, J. Opt. Soc. Am. A **1** (1984), 612.
[11] Y. Gao, W. Hu, S. Xin, and L. Sun, A review of applications of CT imaging on fiber reinforced composites, J. Compos. Mater. **56** (2021), 133–164.
[12] V. K. Garga and V. O’Shaughnessy, Tire-reinforced earthfill. Part 1: Construction of a test fill, performance, and retaining wall design, Can. Geotechn. J. **37** (2000), 75–96.

[13] S. Hasan, V. Niasar, N. Karadimitriou, J. Godinho, N. Vo, S. An, A. Rabbani, and H. Steeb, Direct characterization of solute transport in unsaturated porous media using fast X-ray synchrotron microtomography, Proc. Natl. Acad. Sci. **117** (2020), 23443–23449.

[14] T. C. Heimdahl and A. Drescher, Elastic anisotropy of tire shreds, J. Geotechnical Geoenviron. Eng. **125** (1999), 383–389.

[15] S. Hɪnɪslɪoğlu and E. Ağar, Use of waste high density polyethylene as bitumen modifier in asphalt concrete mix, Mater. Lett. **58** (2004), 267–271.

[16] P. Iassonov, T. Gebrenegus, and M. Tuller, Segmentation of X-ray computed tomography images of porous materials: A crucial step for characterization and quantitative analysis of pore structures, Water Resources Res. **45** (2009), 1–12.

[17] X. Jia, C. Caroli, and B. Velicky, Ultrasound propagation in externally stressed granular media, Phys. Rev. Lett. **82** (1999), 1863–1866.

[18] X. Jia and P. Mills, Sound propagation in dense granular materials, Powders Grains **2001** (2001), 105–112.

[19] A. C. Kak and M. Slaney, Principles of computerized tomographic imaging (classics in applied mathematics), Society of Industrial and Applied Mathematics (1987).

[20] S. Karimpouli, P. Tahmasebi, H. L. Ramandi, P. Mostaghimi, and M. Saadatfar, Stochastic modeling of coal fracture network by direct use of micro-computed tomography images, Int. J. Coal Geol. **179** (2017), 153–163.

[21] H. K. Kim and J. C. Santamarina, Sand-rubber mixtures (large rubber chips), Can. Geotechn. J. **45** (2008), 1457–1466.

[22] O. Kodym and M. Španěl, *Semi-automatic CT image segmentation using random forests learned from partial annotations*, Proc. 11th Int. Joint Conf. Biomed. Eng. Syst. Technol. BIOIMAGING, 2018:124-131; SciTePress.

[23] N. Kotwaliwale, K. Singh, A. Kalne, S. N. Jha, N. Seth, and A. Kar, X-ray imaging methods for internal quality evaluation of agricultural produce, J. Food Sci. Technol. **51** (2011), 1–15.

[24] E. N. Landis and D. T. Keane, X-ray microtomography, Mater. Charact. **61** (2010), 1305–1316.

[25] J. H. Lee, R. Salgado, A. Bernal, and C. W. Lovell, Shredded tires and rubber-sand as lightweight backfill, J. Geotechn. Geoenviron. Eng. **125** (1999), 132–141.

[26] J. S. Lee, J. Dodds, and J. C. Santamarina, Behavior of rigid-soft particle mixtures, J. Mater. Civil Eng. **19** (2007), 179–184.

[27] J. S. Lee and J. C. Santamarina, Bender elements: Performance and signal interpretation, J. Geotechn. Geoenviron. Eng. **131** (2005), 1063–1070.

[28] E. Maire, C. L. Bourlot, J. Adrien, A. Mortensen, and R. Mokso, 20 Hz X-ray tomography during an in situ tensile test, Int. J. Fract. **200** (2016), 3–12.

[29] E. Maire and P. J. Withers, Quantitative X-ray tomography, Int. Mater Rev **59** (2013), 1–43.

[30] A. Misra and N. Nejadsadeghi, Longitudinal and transverse elastic waves in 1D granular materials modeled as micromorphic continua, Wave Motion **90** (2019), 175–195.

[31] R. Mizutani and Y. Suzuki, X-ray microtomography in biology, Micron **43** (2012), 104–115.

[32] O. Mouraille and S. Luding, Sound wave propagation in weakly polydisperse granular materials, Ultrasonics **48** (2008), 498–505.

[33] V. F. Nesterenko, Propagation of nonlinear compression pulses in granular media, J. Appl. Mech Tech. Phys. **24** (1984), 733–743.

[34] Object Research Systems (ORS) Inc, Dragonfly 3.1 (computer software)., Montreal, Canada. http://www.theobjects.com/dragonfly.

[35] J. O'Donovan, C. O'sullivan, G. Marketos, and D. M. Wood, Analysis of bender element test interpretation using the discrete element method, Granul. Matter **17** (2015), 197–216.

[36] N. Otsu, A threshold selection method from gray-level histograms, IEEE Trans. Syst. Man Cybern. **9** (1979), 62–66.

[37] P. S. Rahimabadi, M. Khodaei, and K. R. Koswattage, Review on applications of synchrotron-based X-ray techniques in materials characterization, X-Ray Spectrom **49** (2020), 348–373.

[38] M. Ruf and H. Steeb, An open, modular, and flexible micro X-ray computed tomography system for research, Rev. Sci. Instr. **91** (2020), 113102.

[39] M. Ruf, K. Taghizadeh, and H. Steeb, 2021. Micro-XRCT data sets and in situ measured ultrasonic wave propagation of a pre-stressed monodisperse rubber and glass particle mixture with 50% volume rubber content. DaRUS. https://doi.org/10.18419/darus-2208.

[40] J. C. Russ and F. B. Neal, *The image processing handbook*, 7th ed., CRC Press, Boca Raton, FL, 2016.

[41] P. Russo, Ed., *Handbook of X-ray imaging: Physics and technology*, CRC Press, Boca Raton, FL, 2018.

[42] J. Santamarina and M. Aloufi, Small strain stiffness: A micromechanical experimental study, Proc. Pre-Failure Deform. Char. Geomater. **1** (1999), 451–458.

[43] A. Sawangsuriya, "*Wave propagation methods for determining stiffness of geomaterials*," *Wave processes in classical and new solids*, edited by London, IntechOpen, London, UK, 2012, pp. 157–200.

[44] S. Schlüter, A. Sheppard, K. Brown, and D. Wildenschild, Image processing of multiphase images obtained via X-ray microtomography: A review, Water Resources Res. **50** (2014), 3615–3639.

[45] L. Schoeman, P. Williams, A. du Plessis, and M. Manley, X-ray micro-computed tomography (μCT) for non-destructive characterisation of food microstructure, Trends Food Sci. Technol. **47** (2016), 10–24.

[46] J. Serra, Introduction to mathematical morphology, Comput. Vision, Graph. Image Process. **35** (1986), 283–305.

[47] R. K. Shrivastava and S. Luding, Effect of disorder on bulk sound wave speed: A multiscale spectral analysis, Nonlinear Processes Geophys. **24** (2017), 435–454.

[48] R. Siddique and T. R. Naik, Properties of concrete containing scrap-tire rubber–An overview, Waste Manag. **24** (2004), 563–569.

[49] S. S. Singh, J. J. Williams, P. Hruby, X. Xiao, F. D. Carlo, and N. Chawla, In situ experimental techniques to study the mechanical behavior of materials using X-ray synchrotron tomography, Integr. Mater. Manuf. Innovat. **3** (2014), 109–122.

[50] E. Somfai, J. N. Roux, J. H. Snoeijer, M. Van Hecke, and W. Van Saarloos, Elastic wave propagation in confined granular systems, Phys. Rev. E **72** (2005), 021301.

[51] S. R. Stock, *MicroComputed tomography: Methodology and applications*, CRC Press, Boca Raton, FL, 2008.
[52] S. R. Stock, Recent advances in X-ray microtomography applied to materials, Int. Mater. Rev. **53** (2008), 129–181.
[53] K. Taghizadeh, R. K. Shrivastava, and S. Luding, Stochastic model for energy propagation in disordered granular chains, Materials **14** (2021), 1815.
[54] K. Taghizadeh, H. Steeb, and S. Luding, Energy propagation in 1D granular soft-stiff chain, EPJ Web Conf. **249** (2021), 02002.
[55] K. Taghizadeh, H. Steeb, S. Luding, and V. Magnanimo, Elastic waves in particulate glass-rubber mixtures, Proc. Royal Soc. A **477** (2021), 20200834.
[56] K. Taghizadeh, H. Steeb, V. Magnanimo, and S. Luding, Elastic waves in particulate glass-rubber mixture: Experimental and numerical investigations/studies, EPJ Web Conf. **140** (2017), 12019.
[57] M. Tuller, R. Kulkarni, and W. Fink, "*Segmentation of X-ray CT data of porous materials: A review of global and locally adaptive algorithms*," *Soil–water–root processes: Advances in tomography and imaging*, John Wiley & Sons, Hoboken, NJ, 2013, pp. 157–182.
[58] S. Van den Wildenberg, A. Tourin, and X. Jia, Sound velocity fluctuations in confined granular materials: Coarse-graining lengths and elastic heterogeneities, EPL (Europhys. Lett.) **115** (2016), 34005.
[59] L. Vincent and P. Soille, Watersheds in digital spaces: An efficient algorithm based on immersion simulations, IEEE Trans. Pattern Anal. Mach. Intell. **13** (1991), 583–598.
[60] J. Vlassenbroeck, M. Dierick, B. Masschaele, V. Cnudde, L. Van Hoorebeke, and P. Jacobs, Software tools for quantification of X-ray microtomography at the UGCT, Nucl. Instr. Methods Phys. Res. Sect. A Acceler. Spectrom. Detect. Assoc. Equip. **580** (2007), 442–445.
[61] F. Xiao, S. Amirkhanian, and C. H. Juang, Rutting resistance of rubberized asphalt concrete pavements containing reclaimed asphalt pavement mixtures, J. Mater. Civil Eng. **19** (2007), 475–483.
[62] C. Zhai, E. B. Herbold, and R. C. Hurley, The influence of packing structure and interparticle forces on ultrasound transmission in granular media, Proc. Natl. Acad. Sci. **117** (2020), 16234–16242.
[63] J. G. Zornberg, A. R. Cabral, and C. Viratjandr, Behaviour of tire shred sand mixtures, Can. Geotechn. J. **41** (2004), 227–241.

How to cite this article: M. Ruf, K. Taghizadeh, and H. Steeb, *Multi-scale characterization of granular media by in situ laboratory X-ray computed tomography*, GAMM-Mitteilungen. **45** (2022), e202200011. https://doi.org/10.1002/gamm.202200011